Dynamics of isolated vortex cavitation

P. C. Pennings[1,2,†], **J. Bosschers**[3], **J. Westerweel**[2] **and T. J. C. van Terwisga**[1,3]

[1]Department of Mechanical Maritime and Materials Engineering, Laboratory for Ship Hydrodynamics, Delft University of Technology, Mekelweg 2, Delft 2628 CD, The Netherlands

[2]Department of Mechanical Maritime and Materials Engineering, Laboratory for Aero and Hydrodynamics, Delft University of Technology, Mekelweg 2, Delft 2628 CD, The Netherlands

[3]Maritime Research Institute Netherlands, Haagsteg 2, Wageningen 6708 PM, The Netherlands

The dynamic behaviour of vortex cavitation on marine propellers may cause inboard noise and vibration, but is not well understood. The main goal of the present study is to experimentally analyse the dynamics of an isolated tip vortex cavity generated at the tip of a wing of elliptical planform. Detailed high-speed video shadowgraphy was used to determine the cavity deformations in combination with force and sound measurements. The cavity deformations can be divided in different modes, each of which show a distinct dispersion relation between frequency and wavenumber. The dispersion relations show good agreement with an analytical formulation. Finally, experimental support is given to the hypothesis that the resonance frequency of the cavity volume variation is related to a zero group velocity.

---

1. Introduction

Tip vortex cavitation is among the first forms of cavitation to appear on ship propellers and is an important design consideration for ships that require low noise and vibration levels. The vortex strength and thus the cavity thickness can be reduced by unloading the blade tip at the cost of reduced propeller efficiency. Vortex cavitation may cause broadband hull-pressure fluctuations that can lead to onboard noise and vibrations.

The broadband character can be explained by the variability of the hull pressure fluctuations between blade passages. The centre frequency of the broadband hump is expected to be due to a tip vortex cavity resonance (Ræstad 1996; Bosschers 2007), but this resonance behaviour is not understood. An example of a wing with a tip vortex cavity is shown in figure 6. As early as 1880, a theoretical dispersion relation was derived by Thomson (1880) that describes the dynamics of waves travelling on an isolated tip vortex cavity. This was extended to include the effects of compressibility and surface tension by Morozov (1974). A modification to the theory was proposed by

† Email address for correspondence: p.c.pennings@tudelft.nl

Bosschers (2008, 2009) to account for a free stream axial velocity and viscous effects. As the model for waves on a vortex cavity is neutrally stable there is no obvious criterion at which resonance can be expected.

Experiments involving sound measurements of cavitating tip vortices of wings have shown distinct tonal frequencies (Higuchi, Arndt & Rogers 1989; Astolfi *et al.* 1998). Briançon-Marjollet & Merle (1997) measured the velocity distribution, the cavity diameter and sound of a tip vortex cavity trailing from a wing. A correlation of the sound measurements was made to the frequency of the centreline displacement mode and the elliptic deformation mode in the limit of small wavenumbers as given by Morozov (1974). However, as no high-speed video recordings were available the sound could not directly be related to vortex cavity deformations.

The most detailed study to date is by Maines & Arndt (1997) who used high-speed video recordings to investigate the relation between deformations of a tip vortex cavity and a distinct frequency component in the measured sound. The resonance frequencies obtained from sound measurements were related to a criterion with zero phase velocity but the high-speed video data for this study was also not sufficient to validate the analytic model used to explain the tip vortex cavity resonance frequency. An alternative explanation was provided by Bosschers (2009) who related the experimental data to the criterion of zero group velocity of the mode involving cavity volume variations. A group-speed criterion was used by Keller & Escudier (1980) to explain the occurrence and wavelengths of standing waves on a cavitating vortex in a vortex tube.

This shows that there is a disagreement in the deformation mode which is thought to be responsible for the vortex cavity resonance. The underlying theoretical dispersion relation which is used to describe this criterion varies slightly between authors but has never been validated. The main goal of the present paper is to provide an understanding of the dynamics of waves on a tip vortex cavity by computing a frequency–wavenumber diagram for different cavity deformation modes using detailed high-speed video recordings. In this diagram, distinct features can be distinguished with varying phase velocity and group velocity. Most of these features can be related to the theoretical dispersion relation.

The high-speed video observations are made of a tip vortex cavity generated by a stationary wing of elliptical planform in the Delft cavitation tunnel. To also be able to study the criterion of cavity resonance, tests are performed on a wing similar in geometry to the one used by Maines & Arndt (1997).

In the next section the analytical model for vortex cavity deformations is described. Then, the details of the experimental set-up are given. The results are discussed to gain an understanding of the dynamics of the vortex cavity. Based on the results the validity of the analytical model is assessed and used to define the criterion for a cavity resonance frequency. Finally, the differences in findings compared to the previous studies (Higuchi *et al.* 1989; Maines & Arndt 1997; Astolfi *et al.* 1998) are discussed.

2. Theoretical dispersion relation

The starting point for the derivation of the dispersion relation is the convected Helmholtz equation for a disturbance velocity potential $\tilde{\varphi}$ (Howe 2003):

$$\nabla^2 \tilde{\varphi} - \frac{1}{c^2} \left(\frac{\partial}{\partial t} + \boldsymbol{U} \cdot \boldsymbol{\nabla} \right)^2 \tilde{\varphi} = 0, \tag{2.1}$$

in which c corresponds to the speed of sound and U to the free stream velocity vector. The free stream flow needs to be irrotational with a velocity magnitude much smaller than the speed of sound. A cylindrical coordinate system (r, θ, x) will be adopted with a harmonic variation of the disturbance potential given by:

$$\tilde{\varphi} = \phi(r)e^{i(k_x x + n\theta - \omega t)}, \tag{2.2}$$

in which $\phi(r)$ corresponds to a potential that is only a function of radius, k_x corresponds to the axial wavenumber, n is the azimuthal wavenumber (which must be an integer) and ω the angular frequency. Using only the axial free stream velocity component W in U leads to the equation

$$\phi'' + \frac{\phi'}{r} + \left[-k_x^2 - \frac{n^2}{r^2} + \frac{1}{c^2}(\omega - Wk_x)^2 \right] \phi = 0, \tag{2.3}$$

where a prime denotes a derivative with respect to the radius. When introducing the projected acoustic wavenumber in the radial direction k_r defined as

$$k_r^2 = \frac{1}{c^2}(\omega - Wk_x)^2 - k_x^2, \tag{2.4}$$

and considering that the vortex is radiating sound away from the core of the vortex, the solution for the disturbance potential is given by a Hankel function of the first kind:

$$\tilde{\varphi} = \hat{\phi} H_n^1(k_r r)e^{i(k_x x + n\theta - \omega t)}, \tag{2.5}$$

in which $\hat{\phi}$ is the amplitude of the disturbance potential.

The velocity components in U should include both the axial free stream velocity and the azimuthal velocity due to the vortex, but the addition of an azimuthal velocity leads to a Matthieu equation for which no analytical solution is available. For low frequencies and the typical vortex strengths used here, the additional terms are small for modes $n = 1$ and $n = 2$ as the velocity is divided by the speed of sound and are here neglected. For the mode $n = 0$ no additional terms arise. The introduction of the azimuthal velocity then gives an identical equation to (2.3).

The distortion of the cavitating vortex with average radius r_c is described by a number of modes characterised by k_x, n, ω and amplitude $\hat{r}$. For small amplitudes, the local cavity radius η is given by

$$\eta = r_c + \tilde{r} = r_c + \hat{r}e^{i(k_x x + n\theta - \omega t)}. \tag{2.6}$$

The mode $n = 0$ corresponds to a breathing mode and involves volume variations. Mode $n = 1$ corresponds to a serpentine mode, also called bending mode, helical mode or displacement mode, as it is the only mode that leads to a displacement of the vortex centreline. The mode $n = 2$ is the bell mode or double helix or fluted mode, and leads to an elliptical shape of the vortex core. A visualisation of the modes is presented in figure 1. The distortions are transversely propagating inertial waves and are often referred to as Kelvin waves (Saffman 1995).

The equations to find the dispersion relation are obtained by using a small perturbation analysis for the kinematic and dynamic boundary conditions. The small perturbation in cavity radius with amplitude $\tilde{r}$ will result in a perturbation velocity given by the spatial derivative of the potential $\tilde{\varphi}$. The derivations by Thomson (1880)
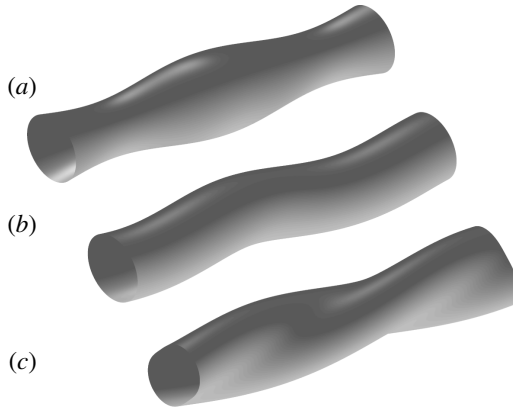
FIGURE 1. Main vortex cavity oscillation modes reproduced from Bosschers (2008). With (*a*) monopole breathing $n = 0$ mode, (*b*) dipole serpentine $n = 1$ centreline displacement mode and (*c*) quadrupole helical $n = 2$ mode.

and Morozov (1974) use a formulation for the azimuthal velocity V valid for potential flow, but we show here that, at least for $n = 0$, the dispersion relation can also be derived for a viscous vortex formulation. In both formulations a zero mean radial velocity U and a constant mean axial velocity component W are used. The mean velocities for potential flow in which a vortex with circulation Γ is present are then given by

$$\boldsymbol{U} = (U, V, W) = \left(0, \frac{\Gamma}{2\pi r}, W\right). \tag{2.7}$$

For viscous flow, the situation is more complicated. Neglecting the flow inside the cavity, the azimuthal velocity in a viscous fluid has to satisfy a zero shear stress boundary condition at the cavity interface, which leads to a different behaviour of the velocity near the cavity interface when compared to the non-cavitating vortex as shown in Bosschers (2015). However, this change in velocity leads to a small change in pressure at the cavity radius from which it is concluded that a formulation for the azimuthal velocity of a non-cavitating vortex can also be used to find the relation between cavity size and pressure. We will use here the Burnham–Hallock model (Burnham & Hallock 1982) due its simple formulation for the pressure variation. The azimuthal velocity at radius r for a vortex with viscous core radius r_v is given by

$$V = \frac{\Gamma}{2\pi} \frac{r}{r_v^2 + r^2}. \tag{2.8}$$

The kinematic boundary condition for $f = r - \eta$ is given by

$$\frac{\mathrm{D}f}{\mathrm{D}t} = \frac{\partial f}{\partial t} + (\boldsymbol{U} + \nabla\tilde{\varphi}) \cdot \nabla f = 0. \tag{2.9}$$

Only the linear terms of the perturbations in potential and cavity radius will be retained, which implies that the equation contains only the perturbation velocity in the radial direction and the derivative of the η perturbation in time, axial direction and azimuthal direction:

$$\hat{\phi}\, k_r H_n^{1'}(k_r r_c) - \left(-\mathrm{i}\omega + W\mathrm{i}k_x + V_c \frac{\mathrm{i}n}{r_c}\right)\hat{r} = 0, \tag{2.10}$$

where the prime again denotes the derivative to r and V_c is the mean azimuthal velocity at the cavity interface $r = r_c$.

The dynamic boundary condition states that the pressure at the cavity interface has to be equal to the vapour pressure. For potential flow, the Bernoulli equation can be used as done in Thomson (1880) and Morozov (1974). Here, we will start from the radial momentum equation to investigate if a viscous vortex solution can be applied. The radial momentum equation is given by

$$-\frac{1}{\rho}\frac{\partial p}{\partial r} = \frac{\partial}{\partial t}\frac{\partial \tilde{\varphi}}{\partial r} + (\boldsymbol{U} + \boldsymbol{\nabla}\tilde{\varphi}) \cdot \boldsymbol{\nabla}\frac{\partial \tilde{\varphi}}{\partial r} - \frac{\left(V + \dfrac{\partial \tilde{\varphi}}{r\partial\theta}\right)^2}{r}. \tag{2.11}$$

If we take only the linear terms into account, the equation reads:

$$-\frac{1}{\rho}\frac{\partial p}{\partial r} = \frac{\partial}{\partial t}\frac{\partial \tilde{\varphi}}{\partial r} + W\frac{\partial}{\partial x}\frac{\partial \tilde{\varphi}}{\partial r} + V\frac{\partial}{r\partial\theta}\frac{\partial \tilde{\varphi}}{\partial r} - \frac{V^2}{r} - \frac{2V}{r}\frac{\partial \tilde{\varphi}}{r\partial\theta}. \tag{2.12}$$

The first two terms on the right-hand side can be directly integrated. The third and fifth terms on the right-hand side can only be integrated if a potential flow solution is assumed for V, but these terms vanish for the mode $n = 0$ as the azimuthal disturbance velocity equals zero for this mode. The fourth term can be integrated using either (2.7) or (2.8) for the azimuthal velocity. The integration for this fourth term using (2.8) gives for the pressure in the liquid at the cavity interface $r = \eta$:

$$p_v - p_T + \frac{1}{2}\rho\left(\frac{\Gamma}{2\pi}\right)^2 \frac{1}{(r_v^2 + \eta^2)} = p_\infty, \tag{2.13}$$

where p_v corresponds to the vapour pressure, p_T to the contribution of surface tension and p_∞ to the free stream pressure in absence of the vortex. Assuming a small amplitude $\tilde{r}$ with respect to r_c, the equation can be written as

$$p_v - p_T + \frac{1}{2}\rho\left(\frac{\Gamma}{2\pi}\right)^2 \frac{1}{(r_v^2 + r_c^2)} - \rho\left(\frac{\Gamma}{2\pi}\right)^2 \frac{\tilde{r}r_c}{(r_v^2 + r_c^2)^2} = p_\infty. \tag{2.14}$$

The contribution due to surface tension T at $r = \eta$ is given by:

$$
\begin{aligned}
p_T &= T\left(\frac{\partial^2}{\partial x^2} + \frac{\partial^2}{\partial r^2} + \frac{1}{r}\frac{\partial}{\partial r} + \frac{1}{r^2}\frac{\partial^2}{\partial\theta^2}\right)(r - [r_c + \tilde{r}]) \\
&= T\left(k_x^2 + \frac{1}{\eta^2}n^2\right)\tilde{r} + T\frac{1}{\eta} \\
&= \frac{T}{r_c}\left[1 + (n^2 + k_x^2 r_c^2 - 1)\frac{\tilde{r}}{r_c}\right],
\end{aligned}
\tag{2.15}
$$

where again a linearisation has been applied for the perturbation of the cavity radius. For the situation with zero perturbation, the difference in pressure between the free stream and at the mean cavity radius due to the mean azimuthal velocity is

$$p_\infty - p_c = \frac{1}{2}\rho\left(\frac{\Gamma}{2\pi}\right)^2 \frac{1}{(r_v^2 + r_c^2)}, \tag{2.16}$$

with the pressure at the cavity interface given by

$$p_v - \frac{T}{r_c} - p_c = 0. \tag{2.17}$$

The contribution of the term containing $\tilde{r}$ in (2.14), referred to as $\tilde{p}_{c,4}$, with subscript 4 referring to the fourth term in (2.14), can be written as:

$$\tilde{p}_{c,4} = \rho \left(\frac{\Gamma}{2\pi} \right)^2 \frac{\tilde{r} r_c}{(r_v^2 + r_c^2)^2} = \rho V_c^2 \frac{\tilde{r}}{r_c}. \tag{2.18}$$

This relation between $\tilde{p}_{c,4}$ and V_c derived for the Burnham–Hallock vortex model is identical to that for a vortex in potential flow given by (2.7), and it will be assumed in the following that this relation is generally valid and can also be used for viscous vortex formulations different from the Burnham–Hallock model.

The sum of all terms in (2.12) containing perturbations to the pressure should be equal to zero, which gives

$$\frac{T}{r_c}(n^2 + k_x^2 r_c^2 - 1)\frac{\tilde{r}}{r_c} - \rho V_c^2 \frac{\tilde{r}}{r_c} + i\rho \left(k_x W + \frac{V_c n}{r_c} - \omega \right) \tilde{\varphi} = 0. \tag{2.19}$$

Combining the kinematic boundary condition (2.10) and the dynamic boundary condition (2.19) leads to the dispersion relation:

$$\omega_{1,2} = W k_x + \Omega \left[n \pm \sqrt{\frac{-k_r r_c H_n^{1'}(k_r r_c)}{H_n^1(k_r r_c)} T_\omega} \right], \tag{2.20}$$

in which $\Omega = V_c/r_c$ and T_ω includes the contribution of the surface tension:

$$T_\omega = \sqrt{1 + \frac{T}{\rho r_c V_c^2}(n^2 + k_x^2 r_c^2 - 1)}. \tag{2.21}$$

Each vibration mode contains two frequencies corresponding to the plus and minus sign on the right-hand side of (2.20). This sign is also used in the following for the identification of the mode. The contribution of the surface tension will not be discussed further as its influence is very small for the case considered. As both frequencies are real numbers the perturbations are neutrally stable. If the axial velocity W is small with respect to the speed of sound, the criterion for a sound wave to occur is that the radial wavenumber squared, defined by (2.4), is larger than zero. This results in the condition

$$\left| \frac{c_{p,x}}{c} \right| = \left| \frac{k}{k_x} \right| > 1, \tag{2.22}$$

where $c_{p,x} = \omega/k_x$ corresponds to the axial phase velocity and k corresponds to the acoustic wavenumber in the fluid, $k = \omega/c$.

For small axial phase velocities or low frequencies the radial wavenumber becomes imaginary and the Hankel function reduces to a modified Bessel function of the
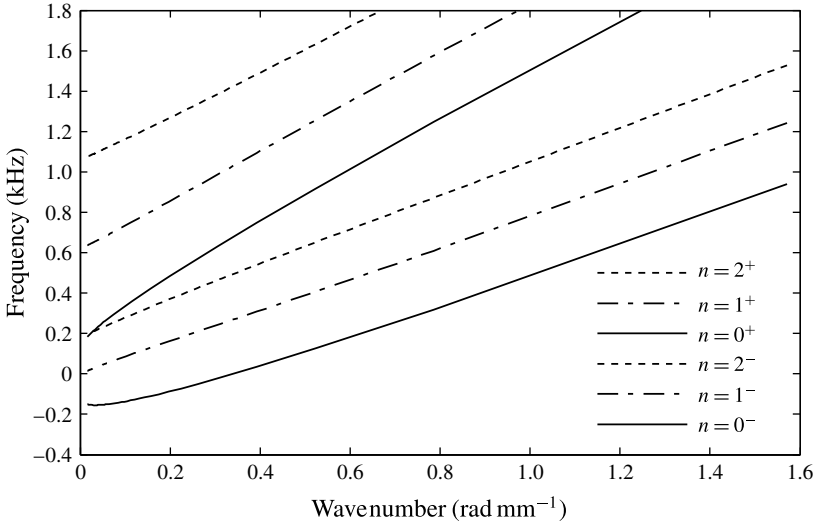
FIGURE 2. Dispersion relation for the two $\pm$ branches of the three modes described by (2.20). Condition; $\Omega = 2.0 \times 10^3$ rad s^{-1}, $W = 6.3$ m s^{-1} and $r_c = 2.3$ mm.

second kind K. The wave in the radial direction now becomes an evanescent wave as $k_r^2 \cong -k_x^2$. The dispersion relation for low frequencies is then given by

$$\omega_{1,2} = Wk_x + \Omega \left[n \pm \sqrt{\frac{-k_x r_c K_n^{1'}(k_x r_c)}{K_n^1(k_x r_c)}} \right], \qquad (2.23)$$

with the non-dimensional form given by

$$\bar{\omega}_{1,2} = \frac{\omega_{1,2} r_c}{W} = \kappa + \frac{V_c}{W} \left[n \pm \sqrt{\frac{-\kappa K_n'(\kappa)}{K_n(\kappa)}} \right], \qquad (2.24)$$

in which a non-dimensional wavenumber $\kappa = k_x r_c \cong i\,k_r r_c$ has been introduced. For low frequencies and small axial velocities, the value of the radial wavenumber becomes approximately equal to the axial wavenumber. An example of the dispersion relation of (2.20) is given in figure 2.

In the present formulation only outgoing waves are considered while reflections from, for instance, the wall of the test-section of the cavitation tunnel may also be present. The potential at the tunnel walls can be computed from (2.5) while assuming an evanescent wave. A typical value of the smallest relevant wavenumber on the tip vortex cavity from figure 2 and as found in the experiment is $k_x = ik_r = 0.04$ rad mm^{-1}. The walls of the tunnel used for the experiment are at a distance $r = 0.15$ m from the tip vortex cavity. This results in a value of $k_r r = 6$ which shows that the influence of the tunnel walls on the dispersion relation can be neglected.

The azimuthal velocity at the cavity interface can be derived from the pressure difference. Neglecting surface tension, the formulation for the potential flow vortex gives:

$$\frac{V_c}{W} = \sqrt{\frac{p_\infty - p_v}{\frac{1}{2}\rho W^2}} = \sqrt{\sigma}. \qquad (2.25)$$

For a viscous flow vortex, the analytical formulation for the azimuthal velocity distribution of a 2-D cavitating vortex is given in Bosschers (2015). The formulation can be interpreted as a cavitating Lamb–Oseen vortex and reads:

$$V = \frac{\Gamma}{2\pi r} \left\{ 1 - \beta \exp\left[-\zeta \frac{(r^2 - r_c^2)}{r_v^2} \right] \right\}, \tag{2.26}$$

with β defined by

$$\beta = \frac{r_v^2}{r_v^2 + \zeta r_c^2}, \tag{2.27}$$

and where ζ is a constant ($\zeta = 1.2564$) defined such that the maximum azimuthal velocity for a non-cavitating vortex occurs on the radius of the viscous core of the non-cavitating vortex, r_v.

The formulation has been derived using the appropriate jump relations for the stresses at the cavity interface which gives a shear stress in the liquid at the cavity interface that is approximately zero. The condition of zero shear stress results in a small region of solid-body rotation near the cavity. The present formulation is different from the Gaussian vortex formulations proposed by Choi & Ceccio (2007) and Choi *et al.* (2009) who introduce an additional parameter that describes the azimuthal velocity at the cavity interface. The formulation for the azimuthal velocity of the cavitating vortex still needs to be validated by detailed flow field measurements.

The equation can be used to derive an analytical expression for the pressure, which is a function of the same parameters. This formulation for the pressure at the cavity radius replaces (2.25) and reads

$$\sigma = \frac{p_\infty - p_v}{\frac{1}{2}\rho W^2} = \frac{\Gamma^2}{2(\pi W r_c)^2} \left\{ \begin{array}{c} \dfrac{1}{2} - \beta e^{-\zeta r_c^2/r_v^2} + \dfrac{\beta^2}{2} e^{-2\zeta r_c^2/r_v^2} \\[2mm] + \dfrac{\beta \zeta r_c^2}{r_v^2} E_1(\zeta r_c^2/r_v^2) \\[2mm] - \dfrac{\beta^2 \zeta r_c^2}{r_v^2} E_1(2\zeta r_c^2/r_v^2) \end{array} \right\}. \tag{2.28}$$

with E_1 the exponential integral. The azimuthal velocity at the cavity radius now corresponds to

$$V_c = \frac{\Gamma}{2\pi r_c} \left\{ \frac{\zeta r_c^2}{r_v^2 + \zeta r_c^2} \right\}. \tag{2.29}$$

This azimuthal velocity can be used in (2.20) and (2.23). It is recognised that the disturbance in the flow due to the cavity deformations is given by a potential flow solution, which is not consistent with the use of a viscous mean flow solution for the kinematic and dynamic boundary conditions. However, as discussed before, the contribution of the azimuthal velocity component to the free stream velocity U is expected to lead to small changes to the disturbance potential, which suggests that the use of a viscous vortex solution instead of a potential flow vortex solution will also lead to small changes to the disturbance potential. The use of a viscous flow solution for V_c in the kinematic and dynamic boundary condition leading to (2.20) and (2.23) is only allowed for $n = 0$ and when the Burnham–Hallock vortex is used. Nevertheless, we here assume that a generic viscous flow solution can be used for all values of n.

The azimuthal velocity of a non-cavitating and cavitating vortex is given in figure 3. The potential flow formulation corresponds to (2.7) and the viscous flow formulation corresponds to (2.26). The velocities are obtained using a single value of Γ and r_v.
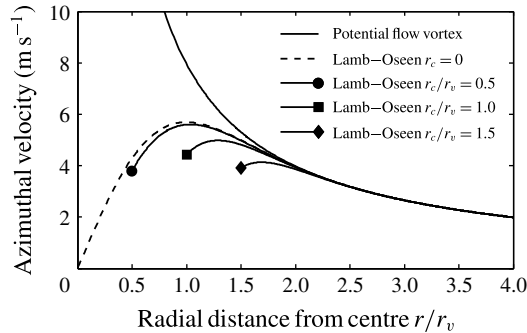
FIGURE 3. Velocity distribution of a potential flow vortex, Lamb–Oseen vortex and three cavitating Lamb–Oseen vortices for $\Gamma = 0.1 \text{ m}^2 \text{ s}^{-1}$ and $r_v = 2$ mm.

3. Experimental set-up

The experimental facility is the cavitation tunnel in the Laboratory for Ship Hydrodynamics at Delft University of Technology. A detailed description of the tunnel is given by Foeth (2008), while the recent modifications are described by Zverkhovskyi (2014).

The maximum free stream tunnel velocity U_∞ is 7 m s^{-1}, which is approximately the velocity used in the results presented here. The cross section is 0.30×0.30 m^2 at the inlet, but changes downstream in vertical direction to 0.30×0.32 m^2 at the outlet to compensate for boundary layer growth, so that there is no streamwise pressure gradient in the test section. A sketch of the set-up is given in figure 4. The coordinate system with the wing tip at the origin is defined with x pointing in the streamwise direction. The top plane (xz) includes the elliptic wing planform with z in the spanwise direction, positive from root to tip. Illumination in the side plane (xy) is partly blocked by the wing mount in the tunnel. The lift direction y is vertically downward.

Tip vortex cavitation is generated by a half-model wing of elliptic planform with an aspect ratio of 3 and a *NACA* 66$_2$–415 cross section with $a = 0.8$ mean line. The trailing edge was truncated at a thickness of 0.3 mm due to manufacturing limitations. The chord length after truncation is 0.1256 m. The wing has a half span of 0.150 m, so that the tip is positioned in the centre of the test section. The wing is mounted with the spanwise direction horizontally, with the suction side pointed downward, on the side window of the test section on a disk containing a six-component force/torque sensor (ATI SI-330-30).

The water temperature is measured with a PT-100 sensor placed in a quiescent corner outside the main flow downstream of the test section. A digital pressure transmitter (Keller PAA 33X) mounted in the throat of the contraction upstream of the test section gives the absolute pressure near the wing at a data acquisition rate of 10 Hz. The free stream tunnel velocity is determined from the pressure drop over the contraction measured with a differential pressure sensor (Validyne DP 15) with a number 36 membrane. Both the values of the absolute pressure sensor and the velocity based on the pressure drop are corrected with a reference measurement using a pitot tube, in an empty test section at the location of the wing.

The dissolved oxygen concentration (DO) was used as a measure of the amount of dissolved gas in the water. A fluorescence-based optical sensor (RDO Pro) was placed in a sample of water taken from the tunnel at the start and end of each day. The typical accuracy of the sensor is 0.1 mg l^{-1}, but due to fluctuations in
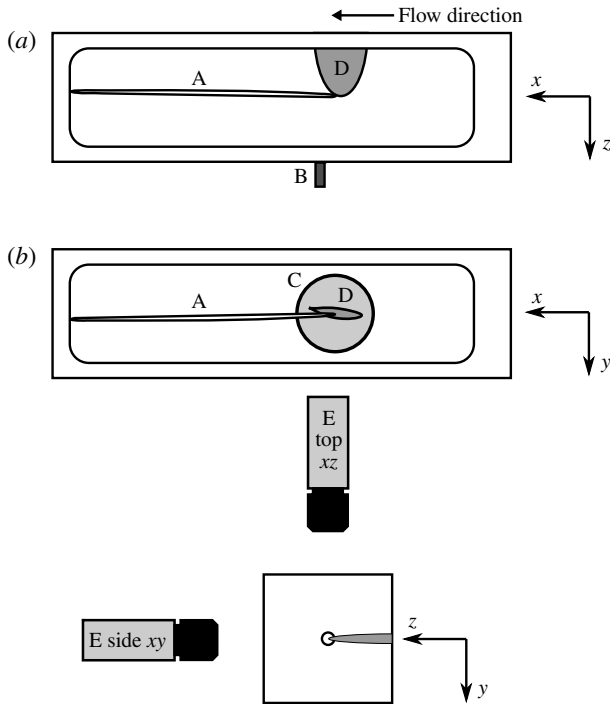
FIGURE 4. Experimental configuration (not to scale) in the cavitation tunnel with tip vortex cavity A, hydrophone B, disk C holding elliptic planform wing D and high-speed cameras E: (*a*) top view, (*b*) side view.

concentration in the tunnel, 0.5 mg l^{-1} is the smallest practical division. As only dissolved oxygen is measured this is taken as a representative indicator for the total amount of dissolved gas.

A hydrophone (Brüel & Kjær type 8103) and a measurement amplifier (Brüel & Kjær type 2606) were used to measure the radiated sound. The hydrophone was inside a water-filled cup mounted on the window opposite the wing at the vertical position of the tip and the streamwise position of the trailing edge. All sensors were sampled at a rate of 40 kHz which is well above the 1.5 kHz upper limit of the relevant frequency range.

Two high-speed cameras (LaVision Imager Pro HS) in combination with two backlight LED panels gave a shadowgraphy image of the tip vortex cavity at 5×10^3 f.p.s. The total recording time, limited by the camera memory, was six seconds. The top view *xz*-plane camera is equipped with a Nikon AF Nikkor 35 mm objective at a *f*-stop value of 2 with an approximate object focal-plane distance of 0.50 m. The disk holding the wing blocks part of the field of view of the side view *xy*-plane camera. Consequently a 55 mm Micro-Nikkor set to *f*-stop of 2.8 is used at a object focal-plane distance of 0.57 m.

Edge detection of the tip vortex cavity is based on gradients in light intensity in the image. A Canny (1986) edge detection method was used with a relative gray value intensity threshold of 0.1 and a filter size of 1.0. Units and detailed description of these parameters can be found in Canny (1986). In the *xz*-plane the tip of the wing is in the field of view and is used to define the origin. As contrast is needed to detect

the cavity edge the detected range is between $x/c_0 = 0.19$ to $x/c_0 = 2.48$ downstream of the tip resulting in an equivalent pixel size of 0.16 mm in the object domain. The edge of the disk holding the wing in the xy-plane is taken as $y = 0$. The cavity extent is between $x/c_0 = 1.12$ and $x/c_0 = 2.60$ downstream of the tip with an equivalent pixel size of 0.10 mm in the object domain. The overlap area between both views where 3-D diameter and location information is available spans $1.35 c_0$.

The pixelization of the diameter and location data are removed by using a fourth order Chebyshev type II low-pass filter. The cut-off frequency was set to half the Nyquist frequency in both cases. The spatial Nyquist frequency is 20 rad mm^{-1} in the xz-plane and 32 rad mm^{-1} in the xy-plane. The low-pass filters were applied in forward and reverse direction to prevent phase shift and to double the effective filter order.

4. Results

The results are presented as follows. First the sensitivity of the mean cavity diameter to dissolved gas and free stream velocity fluctuations is discussed. Second, an overview is given of diameter oscillations in the time domain combined with a description of the stationary cavity geometry. Third, a frequency–wavenumber diagram is generated to validate the analytical model for the dispersion relation. Fourth, a comparison is made between sound, wing forces and cavity oscillations. Finally, the frequency of the peak in the cavity diameter spectrum is compared to the frequency of the zero group velocity criterion that can be derived from the analytical dispersion relation and a comparison is made to the data of the 'singing' vortex as given in Maines & Arndt (1997).

4.1. *Dissolved oxygen concentration*

In the dispersion relation for the vortex cavity the pressure inside the cavity is assumed to be equal to the vapour pressure. Preparations for the test conditions where a steady tip vortex cavity is present can take typically 5 min or more during which the tunnel is in operation. Therefore there is sufficient opportunity for dissolved non-condensable gas to diffuse into the cavity. Figure 5 is the result of a sensitivity study to show the importance of a low dissolved gas concentration to obtain reproducible results. For concentrations below 3.8 mg l^{-1}, the results show acceptably similar values for cavitation numbers above 1.3.

For a cavitation number of 1.1 the standard deviation in core diameter for concentrations of 3.2–3.8 mg l^{-1} is larger than for lower concentrations. The general increase in standard deviation is due to the change of the cavity from a cylindrical shape into a twisted ribbon-like cavity shape as shown in figure 6. At concentrations above 4.0 mg l^{-1} an increase in standard deviation is found for cavitation numbers below 2.2.

The results based on a potential flow vortex give an upper limit to the cavity size as this vortex provides an overestimation of the azimuthal velocity, resulting in a lower pressure and thus a larger cavity. The cavitating Lamb–Oseen model takes the viscous core into account, which reduces the azimuthal velocity and gives a smaller estimate for the diameter, which compares reasonably with the spread in the experimental data.

In the current experiment, the drive system of the cavitation tunnel was run at a constant rotation rate of 700 revolutions min^{-1}. Because of an unidentified flow instability in the tunnel, there are large-scale non-periodic velocity excursions as high as 10 % of the mean. Within the six-second measurement time used, the standard
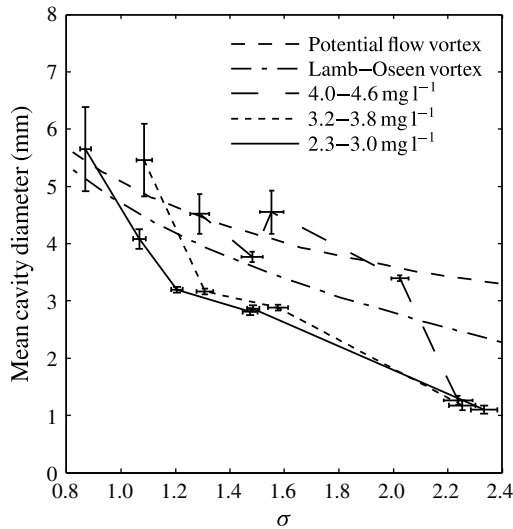
FIGURE 5. Mean cavity diameter in the xz-plane as a function of the cavitation number for a lift coefficient of $C_L = 0.58$ and a Reynolds number based on the wing-root chord of $Re = 9 \times 10^5$. Data points are grouped according to dissolved oxygen concentration. The vertical error bars are the streamwise variation of the time-averaged cavity diameter, which is an indication of the size of the stationary wave amplitude as seen in figure 6. The horizontal error bars denote the variation in cavitation number. The model vortex lines represent the result of (2.25) for a potential flow vortex and (2.28) for a cavitating Lamb–Oseen vortex using $\Gamma = 0.10$ m^2 s^{-1} and $r_v = 1.7$ mm.
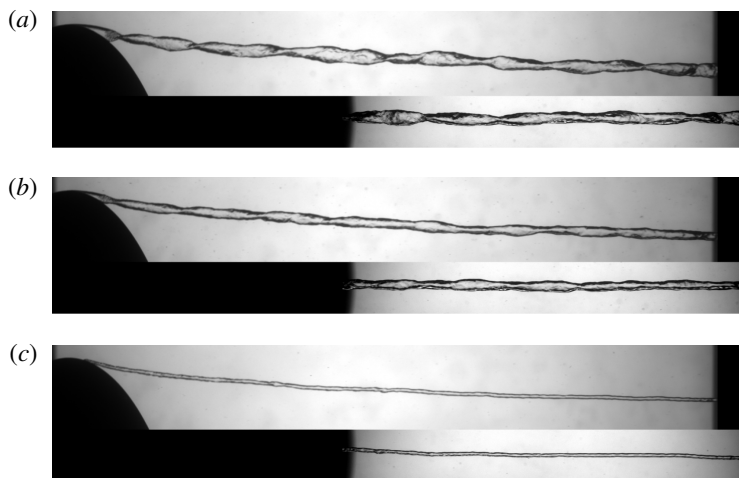
FIGURE 6. Combination of vortex cavity images in xz-plane on top and xy-plane on the bottom of each image. Flow is from left to right with the elliptical black object the pressure side of the wing. (*a*) Conditions; $C_L = 0.58$, $\sigma = 0.87$, $Re = 9.1 \times 10^5$ and $DO = 2.7$ mg l^{-1}. (*b*) Conditions; $C_L = 0.58$, $\sigma = 1.55$, $Re = 9.1 \times 10^5$ and $DO = 4.4$ mg l^{-1}. (*c*) Conditions; $C_L = 0.46$, $\sigma = 1.07$, $Re = 8.9 \times 10^5$ and $DO = 2.7$ mg l^{-1}.

deviation of the velocity in each measurement remained below 5 % with a typical value of 2.5 %. As the fluctuations are not periodic, the time for the flow to meet this condition can vary between measurements. A period with low standard deviation was selected by monitoring the tunnel velocity in real time. The consequence of this approach is a difference between measurements in the time for which the cavity is exposed to over-saturated water.

Long exposure times of the tip vortex cavity to over-saturated water and excursions to lower pressures due to higher free stream velocities promote diffusion of gas into the cavity. This increases the mean cavity diameter and promotes the appearance of a stationary wave for higher cavitation numbers. This is expected to be the cause for the decrease in cavity diameter between $\sigma = 1.6$ and $\sigma = 1.4$ for dissolved oxygen concentrations above 4.0 mg l^{-1} as seen in figure 5.

4.2. *Cavity dynamics in time and frequency domain*

For the detailed evaluation of the cavity dynamics a single condition is selected corresponding to figure 6(*b*). Out of seven cases with significant volume variations, this case shows the largest indication for a cavity eigenfrequency. In this case the dissolved gas in the water is highly over-saturated. For later comparison, the condition of figure 6(*c*) is used. This is at the minimum dissolved gas concentration possible in the cavitation tunnel.

The temporal cavity diameter oscillations are expected to be a combination of the $n = 0^{\pm}$ and $n = 2^{\pm}$ modes as presented in figure 1. As two separate views are available, the identification has to be made by combining both views. Figure 7 shows a colour coded tip vortex cavity diameter for the *xz*-plane in the top figure and *xy*-plane in the bottom figure over a time span of 0.2 s.

As is already evident from figure 6(*b*), both views in figure 7 show stationary wave patterns for the two cameras with 180° phase difference. This could be interpreted as a cavity with an elliptical shape with the axes rotating in the downstream direction. From a single view this shape is similar to a standing wave, but as the frequency of oscillation is zero it is actually a stationary wave. To guide the eye a black line is drawn with a slope corresponding to a velocity 19 % higher than the free stream velocity U_{∞}. This value results from the analysis of figure 10(*a*). The peak values of diameter seem to be convected with a velocity close to this value. The increase in axial velocity with respect to the free stream velocity near the core is due to the favorable pressure gradient generated by the roll-up of the wing vorticity increasing tip vortex circulation. High C_L and small r_c values give increased axial velocities.

The graphs on the right of figure 7 are averages over the whole spatial domain and present the variation of the spatial mean diameter in time. The general trend over 0.2 s shows that there are low-frequency changes in mean diameter that might be due to changes in free stream velocity, which are of the same time scale. The phase angle between the two planes of the averaged cavity diameter in space is approximately zero.

The dominant stationary wave pattern present on the cavity has a direct relation with the diameter. The values for the maximum cavity diameter and the stationary wavelength are compared in figure 8 with data of Maines & Arndt (1997). In this figure the filled symbols are the current results using the maximum of the time averaged cavity diameter. The general trend is the same for both studies.

A frequency analysis of the diameter variations in time as seen in the *xz*-plane was performed and the results are presented in figure 9 as a function of streamwise distance. As mentioned before this case was specifically selected due to the presence of a tonal frequency component at 170 Hz, which can clearly be detected in the graph.
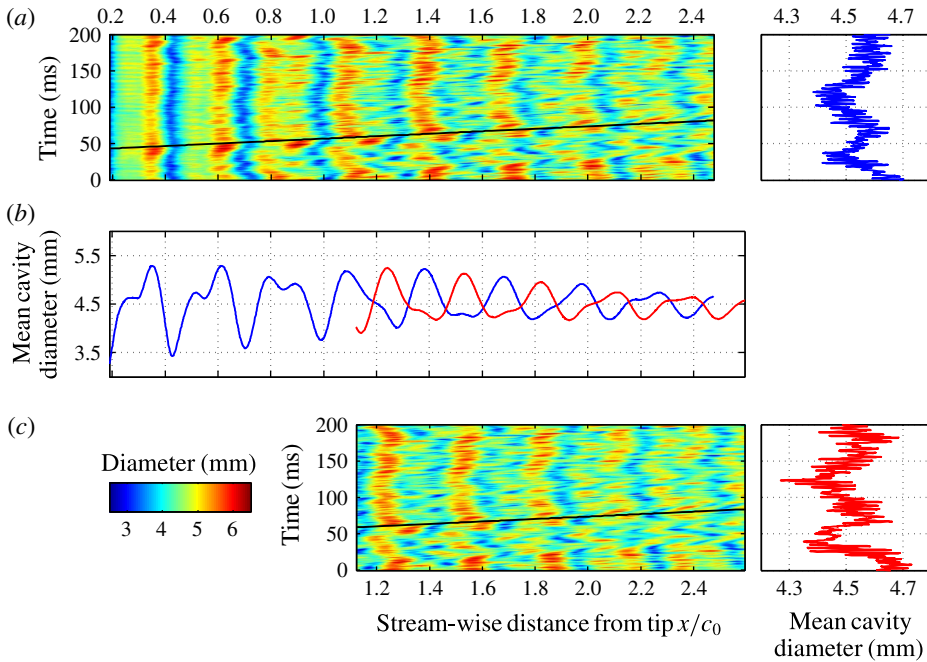
FIGURE 7. Variation of cavity diameter in time and space in the xz-plane on (a) and xy-plane on (c), black line indicates convection at $1.19\,U_\infty$. The graph in (b) is the time averaged diameter with the blue line corresponding to the xz-plane and the red line to the xy-plane. The graphs on the right are the spatial averages. Conditions of figure 6(b).
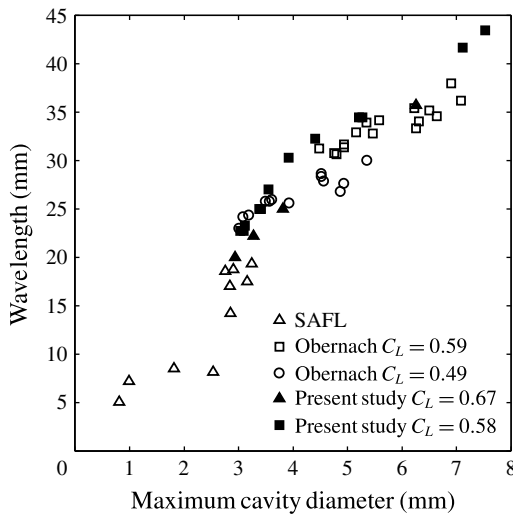
FIGURE 8. Comparison of the wavelength of the stationary cavity shape with maximum cavity diameter, data from Maines & Arndt (1997) at SAFL and Obernach is presented by open symbols and of the present study by filled symbols.
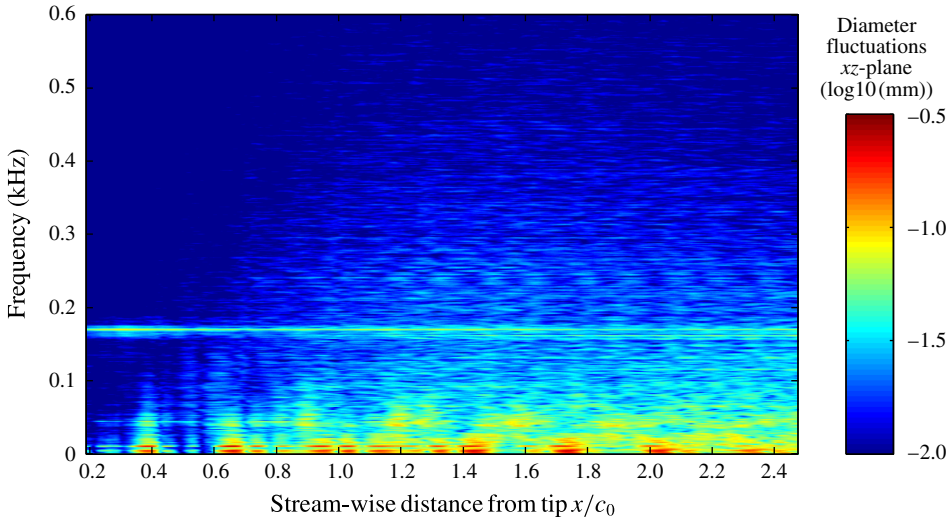
FIGURE 9. Amplitude spectrum of cavity diameter variations. Conditions of figure 6(*b*). The horizontal line corresponds to a high amplitude narrow band frequency component at 170 Hz.

The variation of the diameter amplitude in streamwise direction is smallest close to the tip. Further downstream, the amplitude of the fluctuations increases over a broad frequency range between 0 and 200 Hz. At very low frequencies the contribution of the stationary cavity shape is very large as indicated by the red patches.

4.3. *Cavity dynamics in wavenumber–frequency domain*

Information about the three wave modes comes from the relation between the wavenumber and the frequency of the oscillation which can be obtained from a 2-D fast Fourier transform (FFT) of the high-speed video observations. The $n = 0$ and $n = 2$ modes are related to diameter variations while the $n = 1$ mode is based on motion of the centreline. The $n = 0$ and $n = 2$ modes can be distinguished by the phase difference of the observations in the *xz*-plane and the observations in the *xy*-plane, corresponding to 0° and 180°, respectively. The diameter data from the *xz*-plane is analysed as it captures the largest streamwise variation, hence it provides the highest resolution in wavenumber. The result is given in figure 10(*a*).

Features in the amplitude spectrum and phase spectrum of figure 10 can be understood using the observations of the previous figures. The amplitude of the background disturbance is around 10^{-5} mm while the significant features have an amplitude of 10^{-2} mm. The main feature can be represented by a straight line indicated by the dashed line and cannot directly be related to the dispersion relation of (2.20). The slope of the line is the group velocity $\partial \omega / \partial k_x$. In this case the group velocity is constant and is 19 % faster than the free stream velocity as also observed in figure 7. This can be interpreted as small perturbations present on the cavity which are directly related to disturbances in the free stream. These disturbances are not included in the theoretical model. The faint lines with equal slope are harmonics of this contribution and are the result of the FFT of a signal that is not perfectly sinusoidal. Another notable feature of the line is the location where it crosses the zero
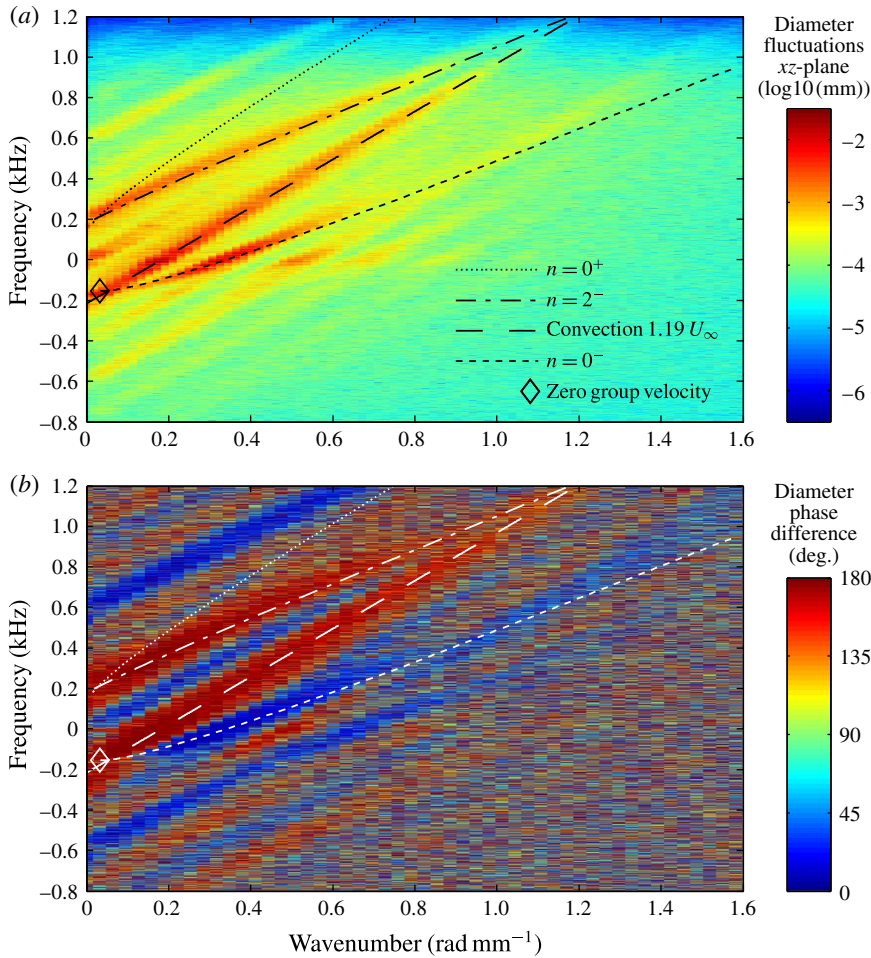
FIGURE 10. Wavenumber–frequency amplitude (*a*) and phase spectrum (*b*) at the condition of figure 6(*b*). Included are the lines for the breathing $n = 0^{\pm}$ and helical $n = 2^{-}$ modes and a line for constant group velocity that is 19 % larger than the tunnel free stream velocity. Derived quantities; $\Omega = 2.0 \times 10^3$ rad s^{-1}, $r_c = 2.3$ mm, $r_v = 1.9$ mm and $\Gamma = 0.10$ m^2 s^{-1}.

frequency axis, at approximately 0.2 rad mm^{-1}. This corresponds to the dominant stationary wave pattern seen in figure 7 and is used for figure 8.

Two other features that are high in amplitude do not correspond to free stream convection. To understand these contributions the lines of the $n = 0^{-}$ and the $n = 2^{-}$ modes of the dispersion relation of (2.20) are matched to the features to obtain the core angular velocity Ω using the mean value for r_c. The positive counterparts of these modes, which can be seen in figure 2, are only shown when present inside the wavenumber–frequency range of the experimental results. The $n = 2^{+}$ mode is therefore not considered at all. From the values of Ω at different cavitation numbers, the local tip vortex circulation and viscous core size can be obtained using a least-squares fit using (2.29). The results are given in the captions and the validity of these numbers will be discussed later.
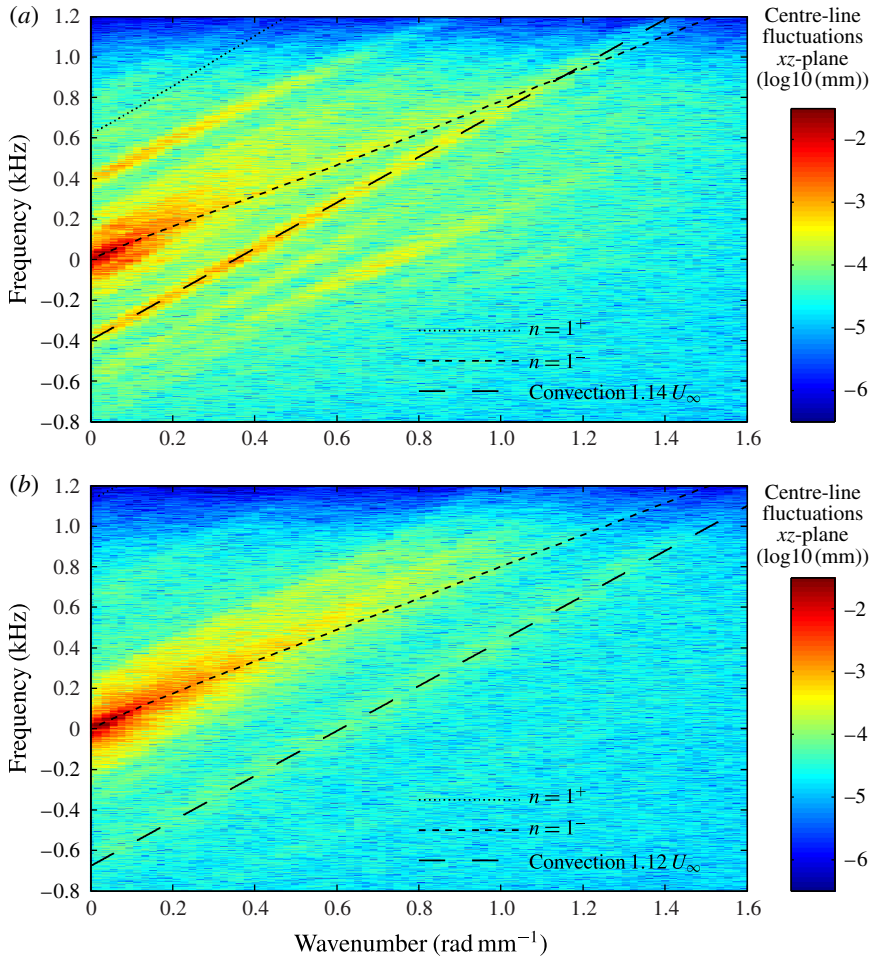
FIGURE 11. Wavenumber–frequency amplitude of centreline fluctuations at the condition of figure 6(*b*) on (*a*) and at the condition of figure 6(*c*) on (*b*). Included are the lines for the serpentine $n = 1^{\pm}$ and a line for constant group velocity that is 14 % and 12 % larger than the tunnel free stream velocity.

The $n = 0^-$ mode follows the feature that crosses the zero-frequency line at the wavenumber of 0.4 rad mm^{-1}. The dash-dotted line is the $n = 2^-$ mode, which is the second to top feature. These modes can be distinguished by the phase difference in diameter between the xz-plane and the xy-plane. The data on the xz-plane is interpolated onto the xy-plane in the area of overlap. The phase difference in the frequency domain between these planes is presented in figure 10(*b*).

Here the same features as in figure 10(*a*) can be identified. The convection contribution has a clear 180° phase difference that can be related to the stationary wave geometry of figure 7. Any other waves superimposed on this do not have high enough amplitude to offset this basis. The harmonics in figure 10(*a*) of this line are present at zero phase difference. These features, with a slope equal to the convection line, are thus clearly disturbances related to the free stream flow.

The feature below this line has a clear zero degree phase difference, which supports that this is the $n = 0^-$ volume variation mode. The other feature, which has a 180°

phase difference, was matched to the $n = 2^-$ mode confirming the effect of the rotation of an ellipsoidal cross section. The $n = 0^+$ mode cannot be identified in either figure 10(a) or 10(b). This could be due to a group velocity that is higher than all other modes and little energy transfer takes place with other modes.

The displacement mode $n = 1$ is evaluated by analysis of the cavity centreline fluctuations. The result is presented in figure 11(a). Here the contributions of convection and its harmonics are dominant. The dashed line has a 14 % larger velocity than the free stream velocity. The uncertainty of estimation of the slope of the convection line is typically ±1 %. The high amplitudes near the origin are mainly due to the mean curved trajectory of the centreline in the streamwise direction. The line originating from here with a smaller slope than the convection line is matched to the $n = 1^-$ line with the same value for Ω as figure 10(a). The $n = 1^+$ mode is not observed in the fluctuations of the centreline.

To determine whether the theoretical dispersion relation is able to predict differences in experimental conditions a comparison to a case with values at the conditions of figure 6(c) is made. This results in a smaller cavity diameter and different cavity dynamics. The identification of the data and the plotted lines in figure 12 is similar to figure 10.

The difference in the value for the convection velocity is related to the local streamwise velocity near the vortex cavity. For a case without cavitation the axial flow in the centre of a vortex core is higher than the free stream (Arndt & Keller 1992). The axial velocity decreases away from the vortex core to the undisturbed free stream value. This results in a higher local axial velocity for a smaller diameter vortex cavity in comparison to a larger diameter vortex cavity and thus a higher convection velocity.

As the stationary wave pattern has a higher wavenumber due to a smaller cavity diameter and thus a higher azimuthal velocity, the zero frequency crossing of the dashed line is around 0.30 rad mm^{-1}. The slope in this case is 12 % higher than the free stream velocity. The theoretical dispersion relation is well able to account for the differences in experimental conditions as seen from the match between the lines and features in the spectrum. The $n = 0^+$ mode is only observed in the phase difference of figure 12(b).

The convection of the centreline disturbances with the free stream velocity is faint in figure 11(b) and slower than the convection in figure 12(a). The amplitude around the origin is more pronounced than in figure 11(a). The amplitude of these centreline waves is small and thus difficult to analyse in the time domain. The fluctuations of the free stream tunnel velocity occurs typically with a 5 s period which is far beyond the time scale used in the present analysis.

The value for the cavity angular velocity that was obtained from the fit of the dispersion relation of (2.20) to the experimental data depends on the value for the axial velocity. The dispersion relations shown in figures 10(a) and 12(a) are obtained by using the undisturbed free stream velocity but the influence of other choices has also been investigated. Main conclusions from this sensitivity study are that the best fit for $n = 2^-$ mode is obtained using the undisturbed free stream velocity while the best fit for $n = 0^-$ mode is obtained using the fitted value for the convection velocity. This results in a lower and upper estimate for the cavity angular velocity shown in figure 13, which differ by approximately 10 %. Both fits give a better agreement than the fits shown in figures 10(a) and 12(a).

This procedure was followed for 12 and 4 measurements at $C_L = 0.58$ and 0.67 respectively, while varying the cavitation number, resulting in a range of cavity radii.
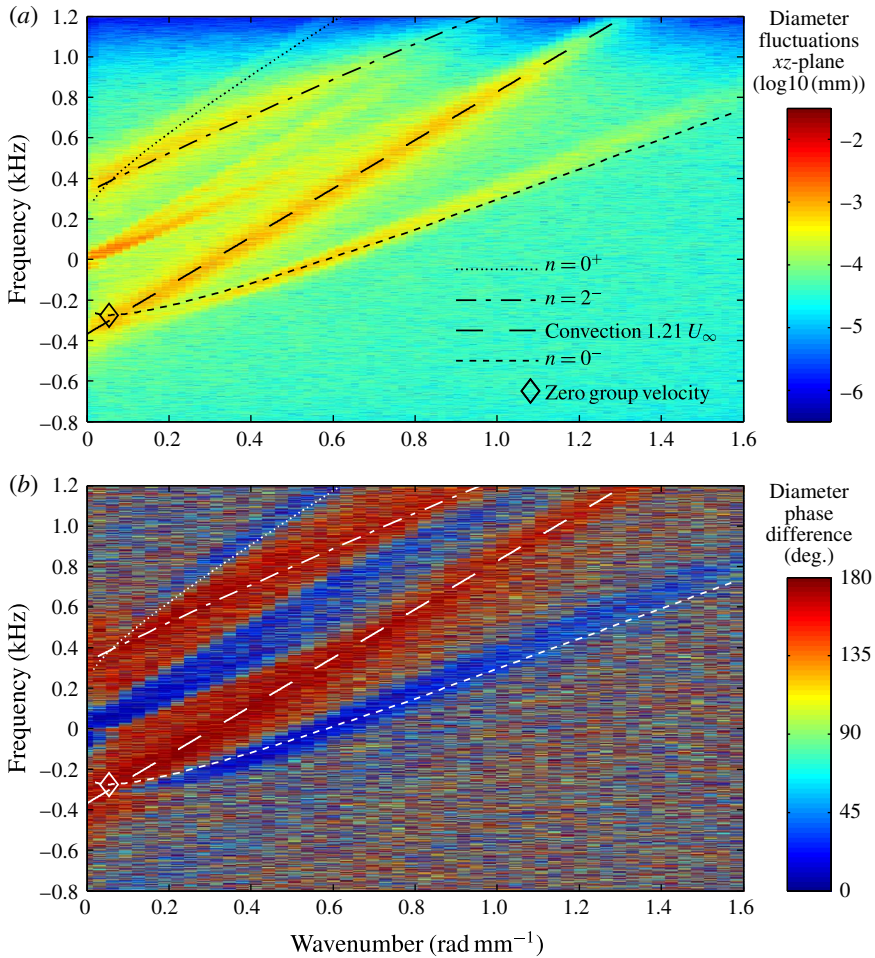
FIGURE 12. Wavenumber–frequency amplitude (*a*) and phase spectrum (*b*) at the condition of figure 6(*c*). Included are the lines for the breathing $n = 0^{\pm}$ and helical $n = 2^{-}$ modes and a line for constant group velocity that is 21 % larger than the tunnel free stream velocity. Derived quantities: $\Omega = 3.6 \times 10^{3}$ rad s^{-1}, $r_c = 1.1$ mm.

The cavitating Lamb–Oseen vortex model of (2.29) was then used to find the values for the vortex circulation and viscous core size. The local tip vortex circulation can be related to the wing root circulation $\Gamma_0 = c_0 C_L U_\infty / 2$ that can be analytically obtained for a wing with elliptic loading distribution. The wing lift coefficient is defined as $C_L = L/(\rho U_\infty^2 S)/2$, where L is the lift force, with wing surface area $S = 1.465 \times 10^{-2}$ m^2. The viscous core size can be related to an equivalent turbulent boundary layer thickness δ of a flat plate with a length equal to the chord of the wing root c_0. Here, $\delta = 0.37 c_0 Re_{c_0}^{-0.2}$ is used, similar to Astolfi, Fruman & Billard (1999). The Reynolds number $Re = U_\infty c_0 / \nu$ is based on the wing root chord c_0 and kinematic viscosity ν. The values for Γ/Γ_0 and r_v/δ for each C_L are given in table 1. The final comparison of the experimental data and the data of the model using the values of table 1 is shown in figure 13. For the determination of these two parameters only the azimuthal velocity of the Lamb–Oseen vortex has been considered. No assumption is made based on the pressure inside the cavity.
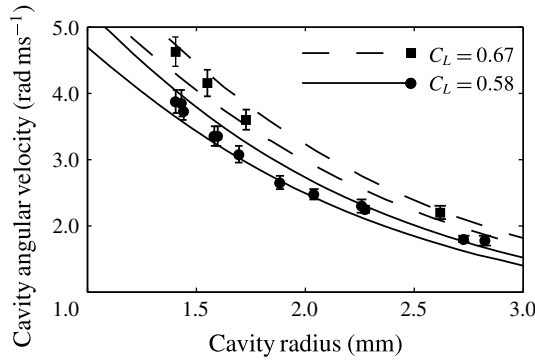
FIGURE 13. Comparison between values of Ω obtained from matching the dispersion relation of (2.20) to the experimental data and the model value lines using (2.29). Bars represent the range between the lower and upper estimate of Ω. Conditions; $C_L = 0.67$, $r_v = 1.7$–1.8 mm, $\Gamma = 0.12$–0.13 m^2 s^{-1} and $C_L = 0.58$, $r_v = 1.7$ mm, $\Gamma = 0.10$–0.11 m^2 s^{-1}.

C_L	0.58	0.67
Γ/Γ_0	0.44–0.47	0.47–0.49
r_v/δ	0.58–0.56	0.61–0.58

TABLE 1. Derived tip vortex characteristics based on matching of dispersion relation of (2.20) to the experimental data in figures 10(a)–12(b). The left and right value correspond to the lower and upper estimate of Ω respectively.

Astolfi *et al.* (1999) found values of $\Gamma/\Gamma_0 = 0.5$–0.6 and $r_v/\delta = 0.8$–1.0 at one chord length downstream of the tip on comparable elliptic planform wings with *NACA* 16020 and *NACA* 0020 airfoil sections. The values for Γ/Γ_0 are very close to the expected range and those for r_v/δ are slightly lower. The latter could be due to the smaller airfoil thickness to chord ratio and the large laminar boundary layer extent for which the presently used *NACA* 66$_2$–415 airfoil section was designed.

4.4. *Sound measurements*

Ten cases showed an indication of the presence of an eigenfrequency in the cavity diameter variations. During the experiments no 'singing' vortex could be heard, in contrast to experiments by others (Higuchi *et al.* 1989; Briançon-Marjollet & Merle 1997; Maines & Arndt 1997; Astolfi *et al.* 1998). The sound spectrum is presented in figure 14 where a comparison is made with the spectrum of forces tangential and normal to the chord line, the cavity diameter and centreline fluctuations.

The 170 Hz peak in the cavity-diameter spectrum does not correspond to any peaks in the spectrum of the sound or force signals. From the bottom graph in figure 14 it is clear that the 170 Hz frequency component is not present in the centreline fluctuations.

The peaks in the spectrum at 220 Hz for the tangential force and at 150 Hz for the normal force are the first two wing eigenfrequencies as determined by applying an impulse load to the wing (under water at rest). This was done approximately 25 times to obtain reliable estimates of the eigenfrequencies.
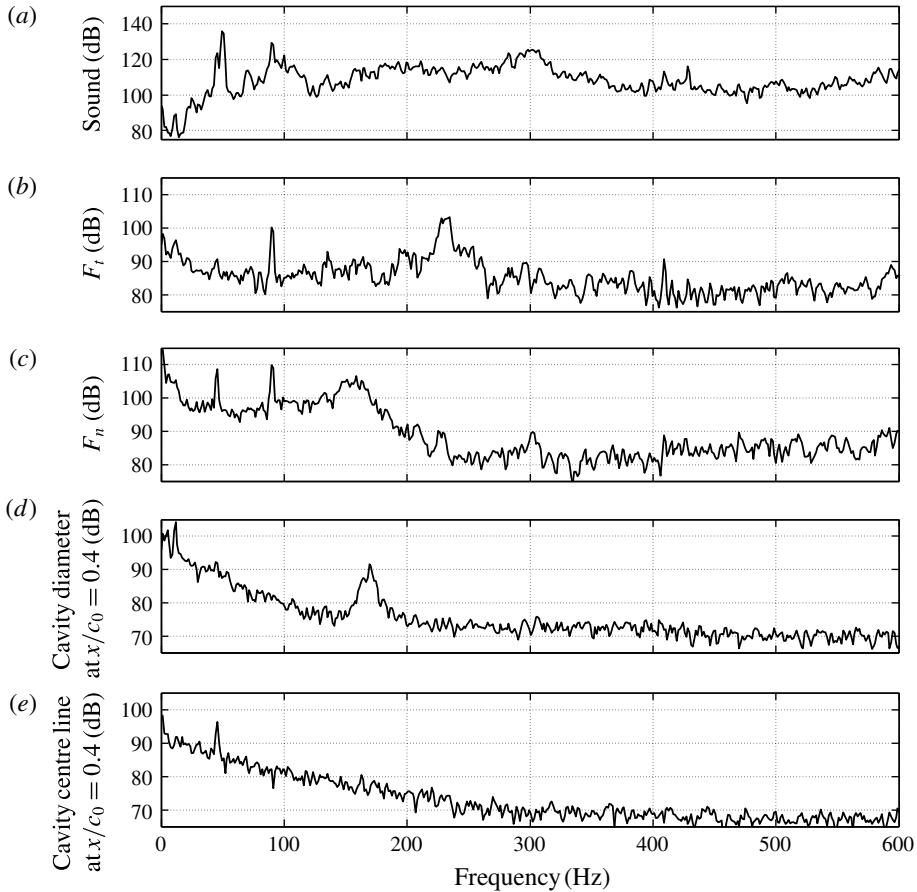
FIGURE 14. Listed from top to bottom a comparison between power density spectra of the sound signal, the force tangential to the wing chord, the force normal to the wing chord, cavity diameter fluctuations and cavity centreline fluctuations. Reference value is 10^{-12} Pa^2 Hz^{-1}, 10^{-12} N^2 Hz^{-1} and 10^{-12} mm^2 Hz^{-1} respectively. Condition of figure 6(*b*).

Several other peaks in the spectra are attributed to the experimental set-up. At 47 Hz the first blade rate harmonic of the four bladed tunnel drive impeller arises with a second harmonic at 94 Hz that are picked up in the sound spectrum, by the force sensor on the wing and by the cavity centreline. At 50 Hz electronic noise from the power supply is picked up. At 300 Hz a more broadband signal caused by cavitation of the tunnel drive impeller is observed. The sound measured in the tunnel without the hydrofoil increases by approximately 30 dB around 300 Hz when increasing the tunnel drive rotation rate from 400 to 700 revolutions min^{-1}. The sound can be identified as cavitation noise by listening at a position close to the tunnel impeller.

The high-amplitude narrow-band frequency component of the cavity diameter fluctuations could not be related to any part of the experimental set-up. It also changes in frequency with cavity size and vortex strength. It is thus likely that it is the cavity resonance frequency for volume variations that is not sufficiently excited to be detected by the hydrophone with the present tunnel background noise.

4.5. *Cavity resonance frequency*

Maines & Arndt (1997) described that the frequency of a 'singing' vortex correlated well with the fluctuations in length of a small cavity sheet but only when the vortex cavity was connected to the tip of the wing. In the current study, the tip vortex cavity was always connected to the wing but was very stable and showed no periodic oscillation to a casual observer. Although no tip instability and no 'singing' vortex sound was observed, figure 14 does show a strong narrow-band component in diameter variations.

The current hypothesis is that a tip vortex cavity has a certain resonance frequency. It can be excited by forcing of deformations with a matching frequency and wavelength resulting in audible sound emission. For the forcing to have a matching characteristic frequency some feedback mechanism should be present. The oscillations of the sheet cavity at the tip generates waves on the vortex cavity that in turn impose the frequency of oscillation on the sheet. This condition requires waves to travel upstream, thus having a negative phase velocity ω/k.

For a strong cavity-wave amplification to occur, wave energy should be contained in space. In the dispersion relation of the $n = 0^-$ mode there exists a criterion at which the velocity of wave energy is zero. This criterion can be identified best in figure 12(*a*) where the slope of this line becomes zero. At this criterion the frequency is negative, thus resulting in a negative phase velocity. The convection line intersects the $n = 0^-$ line at this criterion. The convection velocity is always positive and is thus a potential source for wave energy to be transferred to the $n = 0^-$ mode.

The cavity-diameter spectrum of figure 14 shows that a narrow-band peak is present with a centre frequency of approximately 170 Hz that coincides precisely with the zero group velocity criterion in figure 10(*a*). The centre frequency of the peak in the diameter spectrum is determined for 10 conditions varying in cavitation number and lift coefficient. The result for $C_L = 0.58$ is plotted in figure 15 together with 'singing' vortex data from Maines & Arndt (1997), which were obtained using sound measurements. The lines are based on the dispersion relation model of (2.20) using a potential-flow vortex and the Lamb–Oseen vortex to relate the cavity radius to the cavitation number, similar to Bosschers (2009). The effect of these two models on the relation between the cavitation number and cavity radius was also shown in figure 5.

The potential flow vortex model is acceptable for large cavities, but for small cavities it is essential to include the effect of viscosity for a correct description of the cavity eigenfrequency. This is the main reason why the filled data points do not overlap with the 'singing' vortex cases represented by the open symbols. The Reynolds number *Re* is lower in the present study than the Obernach cases and for an equal *Re* the wing root chord in the present study is larger than the SAFL cases. Both result in lower cavity rotational frequency Ω giving a lower cavity eigenfrequency. The model lines for the present study cases are based on the values in table 1. For the Obernach cases an estimate of Γ was made using the same ratio for Γ/Γ_0 as found in the present study. The value for the viscous core size was estimated based on the best description of the 'singing' vortex frequencies.

Although the description of Ω by the cavitating Lamb–Oseen model is reasonable, as shown in figure 13, there is still an overestimation of the cavity radius with respect to cavitation number as seen in figure 5. The correct modelling of the velocity field around a tip vortex cavity and estimation of the cavity size require improvement which is outside the scope of this paper.
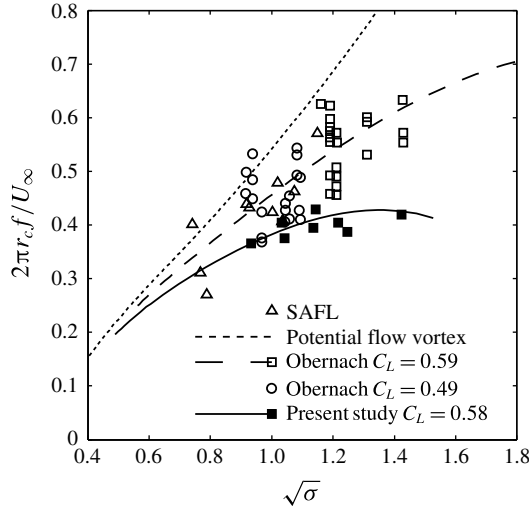
FIGURE 15. Comparison of dimensionless frequency as a function of $\sqrt{\sigma}$ between the data from Maines & Arndt (1997) at SAFL and Obernach in the open symbols and the current results in the filled symbols. The lines are based on the zero group velocity criterion of the $n = 0^-$ mode of (2.20) using either the potential flow vortex or the cavitating Lamb–Oseen vortex. Model quantities Obernach data; $r_v = 1.2$ mm and $\Gamma = 0.20$ m^2 s^{-1}. Model quantities present study; $r_v = 1.7$ mm and $\Gamma = 0.10$ m^2 s^{-1}. For consistency with the dimensionless frequency the results of the lower estimate of Ω in table 1 are used for the model lines.

5. Discussion

The wing geometry used in the study by Maines & Arndt (1997) was used here to study tonal sound emission. As no 'singing' vortex was observed four possible causes were identified that differ between the experiments; dissolved gas, viscous effects on the vortex, wing trailing edge geometry and the boundary layer state.

As mentioned in §4.1 the dissolved gas concentration can affect the mean cavity diameter, which in turn changes the parameters for the cavity deformation dynamics. Unfortunately for some of the experiments a sufficiently low dissolved gas concentration is not possible which implies that a single cavitation number may give different mean cavity diameters as seen in figure 5. The in-gassing only results in a altered pressure difference over the interface thus a bigger cavity and lower angular velocity. This effect is similar to decreasing the free stream pressure or cavitation number of which the influence has been investigated. Because the only relevant vortex parameters in the dispersion relation are the cavity diameter and the cavity angular velocity, the dissolved gas content is not considered to as a plausible cause for the absence of 'singing'.

The experiments in the present study were comparable in size to the Obernach tunnel and in Reynolds number to the experiments in the SAFL tunnel (Maines & Arndt 1997). The consequence of a lower maximum free stream velocity in the Delft facility is that the tunnel free stream pressure needs to be lowered to obtain an equal cavitation number. Without a dedicated degassing system the gas saturation in the water is higher in the present study. A comparison at equal Reynolds number can only be made between cases with different wing size. The larger wing chord and lower

velocity in the present study both contribute to a lower cavity angular velocity, thereby lowering the cavity resonance frequency.

Both the effect of a larger cavity due to gas diffusion into the cavity and the increase of the viscous vortex core can influence the characteristic frequency of the vortex cavity and the sheet cavity at the tip. A repeat test was performed in a different facility to investigate the potential discrepancies. The wing geometry is identical to the one used here but scaled-down to a 0.1125 m span. This was performed at China Ship Scientific Research Center in Wuxi. Only sound measurements and high-speed video observations were performed to be able to identify a 'singing' vortex. After a thorough tunnel degassing procedure without accurate measurement of the dissolved gases, for $C_L = 0.4$–0.6, $Re = 0.6 \times 10^6$–1.5×10^6 and $\sigma = 0.40$–2.60 no sound originating from a 'singing' vortex was observed. So both the dissolved gas concentration and Reynolds number are not considered as the cause for the absence of a 'singing' vortex.

In an early stage of the current experiment a choice was made for the truncation of the trailing edge based on all available information. Unfortunately, the original wing could not be retrieved from the facility in Obernach where part of the experiments of Arndt & Keller (1992) and Maines & Arndt (1997) were performed. The blunt trailing edge with square corners on the current wing is expected to completely eliminate any flow instability near the tip and is thus considered responsible for the absence of a 'singing' vortex in the present experiments. Another potential cause for elimination of the flow instability is the boundary layer state close to the tip. This could be due to the absence of a laminar separation bubble possibly eliminated by surface-roughness induced transition to turbulence.

6. Conclusions

Study of a tip vortex cavity generated by a wing of elliptic planform has provided a fundamental understanding of the cavity interface dynamics. High-speed video recordings from two directions have been used to compute wave number–frequency spectra that clearly show different modes of the cavity diameter and centreline deformations. An analytical model for the dispersion relation of disturbances on an infinite cavitating vortex (Thomson 1880; Bosschers 2008) is matched to the experimental data using values for vortex parameters that are similar to the values found by Astolfi *et al.* (1999). The model describes the relation between wavenumber and frequency over the entire range of experimental data very well. However, not all features in the experimental data are part of the theoretical model such as the stationary ellipsoidal shape of the cross section and the convection of propagations at constant group velocity just above the tunnel free stream velocity.

In all cases with sufficient cavity size, 10 cases were found with a dominant oscillation frequency of the cavity diameter. The value of these frequencies coincides with the location in the dispersion diagram at which the group velocity of the $n = 0^-$ mode is zero. This group velocity criterion also gives a good estimate for the 'singing' vortex frequencies found by Maines & Arndt (1997) for a wing of identical planform and cross section. Despite the presence of a dominant oscillation frequency in the diameter spectra, no cavity sound production was measured under any of the present experimental conditions. It is concluded that a 'singing' vortex does not occur when there is no strong excitation by a flow instability on the wing tip interacting with a vapour cavity.

Acknowledgements

REFERENCES

ARNDT, R. E. A. & KELLER, A. P. 1992 Water quality effects on cavitation inception in a trailing vortex. *Trans. ASME J. Fluids Engng* **114**, 430–438.

ASTOLFI, J.-A., BILLARD, J.-Y., DORANGE, P. & FRUMAN, D. H. 1998 Pressure fluctuations associated with tip vortex and surface cavitation. In *Proceedings of the ASME Fluids Engineering Division Summer Meeting. Washington, DC, USA.*

ASTOLFI, J.-A., FRUMAN, D. H. & BILLARD, J.-Y. 1999 A model for tip vortex roll-up in the near field region of three-dimensional foils and the prediction of cavitation onset. *Eur. J. Mech. (B/Fluids)* **18** (4), 757–775.

BOSSCHERS, J. 2007 Broadband hull pressure fluctuations and cavitating vortices. In *Proceedings of the Ship Noise and Vibration Conference, London, UK.*

BOSSCHERS, J. 2008 Analysis of inertial waves on inviscid cavitating vortices in relation to low-frequency radiated noise. In *Proceedings of the Warwick Innovative Manufacturing Research Centre (WIMRC) Cavitation: Turbo-machinery and Medical Applications Forum.* Warwick University.

BOSSCHERS, J. 2009 Investigation of the resonance frequency of a cavitating vortex. In *Proceedings of the NAG/DAGA International Conference on Acoustics, Rotterdam, The Netherlands.*

BOSSCHERS, J. 2015 An analytical solution for the viscous flow around a 2-D cavitating vortex. *Trans. ASME J. Fluids Engng* (submitted).

BRIANÇON-MARJOLLET, L. & MERLE, L. 1997 Inception, development and noise of a tip vortex cavitation. In *Proceedings of the 21st Symposium on Naval Hydrodynamics.*

BURNHAM, D. C. & HALLOCK, J. N. 1982 Chicago monostatic acoustic vortex sensing system. *Tech. Rep.* DOT-TSC-FAA-79-18, IV. US Department of Transportation.

CANNY, J. 1986 A computational approach to edge detection. *IEEE Trans. Pattern Anal. Mach. Intell.* **8** (6), 679–698.

CHOI, J. & CECCIO, S. L. 2007 Dynamics and noise emission of vortex cavitation bubbles. *J. Fluid Mech.* **575**, 1–26.

CHOI, J., HSIAO, C.-T., CHAHINE, G. & CECCIO, S. 2009 Growth, oscillation and collapse of vortex cavitation bubbles. *J. Fluid Mech.* **624**, 255–279.

FOETH, E.-J. 2008 The structure of three-dimensional sheet cavitation. PhD thesis, Delft University of Technology, Delft, The Netherlands.

HIGUCHI, H., ARNDT, R. E. A. & ROGERS, M. F. 1989 Characteristics of tip vortex cavitation noise. *Trans. ASME J. Fluids Engng* **111**, 495–501.

HOWE, M. S. 2003 *Theory of Vortex Sound.* Cambridge University Press.

KELLER, J. K. & ESCUDIER, M. P. 1980 Theory and observations of waves on hollow-core vortices. *J. Fluid Mech.* **99** (3), 495–511.

MAINES, B. & ARNDT, R. E. A. 1997 The case of the singing vortex. *Trans. ASME J. Fluids Engng* **119**, 271–276.

MOROZOV, V. P. 1974 Theorectical analysis of the acoustic emission from cavitating line vortices. *Sov. Phys. Acoust.* **19** (5), 468–471.

RÆSTAD, A. E 1996 Tip vortex index – an engineering approach to propeller noise prediction. *Nav. Archit.* (July–Aug.), 11–14.

SAFFMAN, P. G. 1995 *Vortex Dynamics*. Cambridge University Press.

THOMSON, S. W. 1880 Vibrations of a columnar vortex. *Phil. Mag.* **10** (61), 155–168.

ZVERKHOVSKYI, O. 2014 Ship drag reduction by air cavities. PhD thesis, Delft University of Technology, Delft, The Netherlands.